Macromolecular-scale resolution in biological fluorescence microscopy

Gerald Donnert*, Jan Keller*, Rebecca Medda*, M. Alexandra Andrei†, Silvio O. Rizzoli‡, Reinhard Lührmann†, Reinhard Jahn‡, Christian Eggeling*, and Stefan W. Hell*§

Departments of *NanoBiophotonics, †Cellular Biochemistry, and ‡Neurobiology, Max Planck Institute for Biophysical Chemistry, 37070 Göttingen, Germany

We demonstrate far-field fluorescence microscopy with a focal-plane resolution of 15–20 nm in biological samples. The 10- to 12-fold multilateral increase in resolution below the diffraction barrier has been enabled by the elimination of molecular triplet state excitation as a major source of photobleaching of a number of dyes in stimulated emission depletion microscopy. Allowing for relaxation of the triplet state between subsequent excitation–depletion cycles yields an up to 30-fold increase in total fluorescence signal as compared with reported stimulated emission depletion illumination schemes. Moreover, it enables the reduction of the effective focal spot area by up to ≈140-fold below that given by diffraction. Triplet-state relaxation can be realized either by reducing the repetition rate of pulsed lasers or by increasing the scanning speed such that the build-up of the triplet state is effectively prevented. This resolution in immunofluorescence imaging is evidenced by revealing nanoscale protein patterns on endosomes, the punctuated structures of intermediate filaments in neurons, and nuclear protein speckles in mammalian cells with conventional optics. The reported performance of diffraction-unlimited fluorescence microscopy opens up a pathway for addressing fundamental problems in the life sciences.

imaging | stimulated emission depletion illumination | subdiffraction | triplet state

For more than a century, the resolution of a lens-based (far-field) optical microscope has been limited by diffraction (1). However, in the 1990s it became evident that the limiting role of diffraction can be broken in lens-based fluorescence microscopy if certain fluorophore properties are judiciously integrated into the image formation (2). The first viable concept of this kind is stimulated emission depletion (STED) microscopy (3), which, since its experimental validation (4, 5), has been key to solving a number of problems in biophysics (6) and cell biology (7, 8).

STED microscopy typically uses a scanning excitation spot that is overlapped with a doughnut-shaped counterpart for deexcitation of fluorophores by light, a phenomenon referred to as stimulated emission (9, 10). Oversaturating the deexcitation squeezes the fluorescence spot to subdiffraction dimensions (Fig. 1a) so that superresolved images emerge by scanning this spot through the object (5).

The rate for deexcitation by stimulated emission is given by $k_{STED} = \sigma I_{STED}$, with σ denoting the fluorophore cross-section and I_{STED} denoting the intensity of the stimulating beam. Oversaturating the deexcitation requires k_{STED} be much larger than the fluorescence decay given by the inverse of the lifetime, $\tau_{Fl} \approx 1$–5 ns, of the fluorescent state S_1. With $\sigma \approx 10^{-17}$ cm^2, it follows that $I_{STED} \gg 1/(\sigma \tau_{Fl}) = 10^{26}$ photons per second per squared centimeter, which, at a wavelength of $\lambda = 600$ nm, amounts to $\hat{I}_{STED} \gg 33$ MW/cm^2. This intensity value is at least 10^3-fold lower than what is required for multiphoton excitation (11), but still 10^2-fold larger than what is used for single-photon fluorescence excitation (3).

Therefore, to operate with a moderate average power, the excitation and the STED beams are implemented as synchro-nized pulse trains (3). The duration of the STED pulse τ_{STED} is adjusted to a fraction of τ_{Fl}, typically ≈0.2 ns, in which case the depletion of the excited state is an exponential function of the stimulating intensity: $\exp[-\sigma \tau_{STED} \cdot I_{STED}]$. Hence, a doughnut-shaped focal distribution $I_{STED}(\vec{r})$ featuring $I_{STED}^{max} \equiv \max[I_{STED}(\vec{r})]$ at the doughnut crest and $I_{STED}(\vec{r} = 0) = 0$ at the center suppresses the signal throughout the focal region, except at $\vec{r} = 0$. The remaining spot in the focal plane follows

$$\Delta r \cong \frac{\lambda}{2n\sin\alpha \sqrt{1 + \sigma\tau_{STED} I_{STED}^{max}}}, \quad [1]$$

with $n \sin \alpha$ denoting the numerical aperture at which the doughnut is generated (12, 13). Thus, provided the doughnut zero is largely maintained, the resolution can be arbitrarily increased with increasing I_{STED}^{max}, in principle, down to the molecular scale (3).

An obvious challenge toward maximizing I_{STED}^{max} is elevated photobleaching of the fluorescent marker that usually scales nonlinearly with the applied intensity (14, 15). For example, at the typical 80-MHz repetition rate of mode-locked lasers, the average focal power applicable to the green dye Atto532 for STED is ≈15 mW (7). The associated $\hat{I}_{STED}^{max} = 250$ MW/cm^2 yields a resolution of $\Delta r = 50$–70 nm. Larger $\hat{I}_{STED}^{max}$ and hence much narrower focal spots were reached only with a red dye under relatively favorable photochemical conditions (13).

In STED microscopy, two bleaching pathways are imaginable (16): (i) the absorption of a fluorescent-state molecule, leading to a higher molecular singlet state, $S_1 \rightarrow S_{x>1}$, as it has been proposed for multiphoton microscopy (17) and (ii) the excitation of excited molecules that have crossed to a triplet state, $T_1 \rightarrow T_{x>1}$, or to another dark state with lifetime $\tau_T > 1$ μs. The states $S_{x>1}$ and $T_{x>1}$ are well known starting points for bleaching reactions (Fig. 1b).

When considering the two routes, it becomes evident that the first one, $S_1 \rightarrow S_{x>1}$, is counteracted by stimulated emission, $S_1 \rightarrow S_0$. With a wavelength optimized for the latter, $S_1 \rightarrow S_{x>1}$ excitation by the STED pulse is less probable. Nevertheless, because the cross-sections for $S_1 \rightarrow S_{x>1}$ are finite both at the STED and at the excitation wavelength, higher singlet excitation is possible. The superexcited $S_{x>1}$ molecule may bleach, cross to the triplet system $S_{x>1} \rightarrow T_{x>1} \rightarrow T_1$, or return to the S_1 (18). Referred to as internal conversion, the last process is very effective because it occurs within a few picoseconds. Because of the STED pulse duration of $\tau_{STED} \approx 0.2$ ns, the putatively superexcited molecule is instantly quenched by the same pulse. Therefore, as long as the molecule remains in the singlet system, the STED pulse is able to protect the molecule from photobleaching.
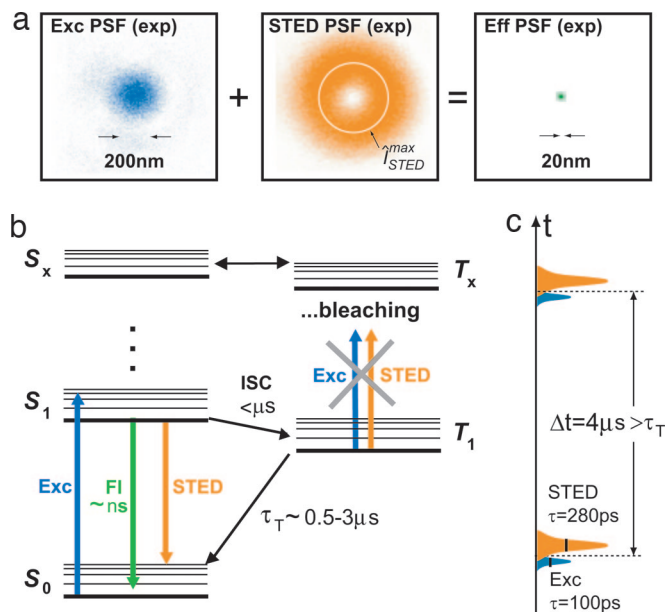

Fig. 1. STED microscopy operation with interpulse time interval Δt. (*a Left* and *Center*) Measured focal spots (PSFs) for excitation (Exc; *Left*) (wavelength, 470 nm; blue) and STED (*Center*) (603 nm, orange). The blue spot of excitation light features a FWHM of 190 nm. (*a Right*) Applying a crest intensity $\hat{I}_{STED}^{max}$ yields the 22-nm effective (Eff) spot shown in green. (*b*) Fluorophore energy levels and potential bleaching pathways. Fluorescence from S_1 is suppressed by stimulated emission. Stimulated emission may also excite the dye to a higher singlet state S_x, from which the molecule can cross to the triplet system T_x. In regions of weak STED pulse intensity, the molecule can directly cross to the T_1 featuring a lifetime $\tau_T = 0.5\text{--}3~\mu s$. Excitation of T_1 molecules by subsequent pulses leads to reverse intersystem crossing or augmented photobleaching. (*c*) These adverse effects are counteracted by $\Delta t > \tau_T$. Note the dramatic reduction in the focal spot area in *a*, resulting from STED.

Just the opposite is the case once the molecule has crossed to the triplet state T_1. Because of its prolonged typical lifetime, $\tau_T \approx 1~\mu s$ at ambient conditions, the T_1 molecule is exposed to a train of intense excitation and STED pulses. Given the rather large molecular cross-sections (10^{-18} to 10^{-17} cm^2) for triplet absorption over a broad wavelength range, the STED pulse can efficiently pump up the molecule to higher triplet states $T_{x>1}$. The ≈80-MHz repetition rate of mode-locked lasers used so far for STED implies that an inherently fragile triplet molecule faces on average 80 intense STED pulses before relaxing to the S_0. Moreover, most fluorophores spontaneously undergo $S_1 \rightarrow T_1$ crossings with a probability of 1–10% per excitation cycle (18). At the doughnut hole, where the STED pulse is weak and the molecules relax spontaneously, stimulated emission does not override the intersystem crossing. Therefore, a remedy against this bleaching pathway is to illuminate molecules as little as possible within the time span $\tau_T \approx 1~\mu s$ after the excitation.

Based on this reasoning, we have explored the operational principles of STED microscopy at a pulse repetition rate of 0.25 MHz that is 320 times lower than the standard rate of 80 MHz. The $\Delta t = 4~\mu s$ time gap between subsequent pulse pairs ensures that most triplet-state molecules of $\tau_T \approx 1~\mu s$ have returned to the ground state before encountering a second or third pulse pair (Fig. 1*c*). We have termed this illumination scheme triplet relaxation (T-Rex) STED.

Results

To explore the potential of T-Rex STED microscopy, we used an optical parametric amplifier fed by a regeneratively amplified mode-locked Ti:sapphire oscillator providing visible pulses of ≈200-fs duration and 100- 250-nJ pulse energy. Note that the

optical setup is detailed in the legend to Fig. 7, which is published as supporting information on the PNAS web site. To stretch the pulses to ≈280 ps by up-chirping, they were diffracted from a pair of gratings before being coupled into a 4-m, single-mode glass fiber. The STED beam was circularly polarized and converted into a doughnut by a spatial phase modulator (Hamamatsu, Hamamatsu City, Japan). The latter was programmed to imprint a helical phase ramp on the STED beam wavefront, $\exp(i\varphi)$ with $0 \leq \varphi \leq 2\pi$ (7); this phase imprint is reminiscent of a Gauss–Laguerre beam providing circular symmetry in the focal plane (19). The central phase singularity of the modified beam coincided with the optical axis. For this study, we excited the dyes with a laser diode emitting ≈80-ps pulses at 470 nm (Picoquant, Berlin, Germany) that was electronically synchronized with the pulses of the STED beam. Both beams were focused by a 1.4 numerical aperture oil immersion lens (Leica Microsystems, Mannheim, Germany) on the sample. Fig. 1*a* shows the measured spot of the blue excitation light along with its STED counterpart.

Reducing the pulse rate by a factor of 320 initially appears unattractive, because the illumination time of the sample per second is reduced accordingly; in other words, the dye is idling more often. Hence, to obtain the same image brightness one would in principle require a 320 times longer recording time. However, experiments comparing the two illumination schemes showed that for the Rhodamine-like dye Atto532 (AttoTec, Siegen, Germany), as well as for other dyes, such as Dyomics485, Atto465, and carboxyl-Rhodamine 6G, this factor is counteracted by a substantial increase of the fluorescence yield.

For example, in the 80-MHz case, the maximum applicable average power on an Atto532-labeled sample was 2 μW for excitation and 15 mW for STED, with corresponding focal intensities of 0.43 MW/cm^2 and $\hat{I}_{STED}^{max} = 250$ MW/cm^2, respectively. In the 0.25-MHz case, we used 0.1 μW for excitation and 0.5 mW for STED, but the lower repetition rate gave rise to a much larger peak power: 7 MW/cm^2 for excitation and $\hat{I}_{STED}^{max} = 2,200$ MW/cm^2. In terms of pulse energy, the individual STED pulse reached a maximum value of 15 mW/80 MHz = 0.1875 nJ in the 80-MHz case and 0.5mW/0.25 MHz = 2 nJ under T-Rex conditions.

Thus, the T-Rex approach not only allowed for 10 times brighter STED pulses but also to excite ground-state molecules 16 times more efficiently per pulse. In fact, we calculated that 17% of all molecules in the inner focal spot were excited to the S_1 by each excitation pulse. With both versions optimized for maximal resolution, the total fluorescence yield per molecule was ≈30 times larger in the T-Rex (0.25 MHz) case than in the corresponding 80 MHz version. Moreover, by better emptying the S_0 and concomitantly increasing the proportion of fluorophores residing in S_1, the strong excitation prepared the grounds for STED.

We first demonstrated the resolution attainable under T-Rex conditions on yellow-green fluorescence beads (Molecular Probes Eugene, OR) emitting in the 500- to 530-nm range (Fig. 2). The fluorophore was not specified, the manufacturer specified the beads to vary by 4 nm around a mean diameter of 24 nm with electron microscopy . The imaging parameters were 10- $\times$ 10-nm pixels, 603-nm STED wavelength, 3-ms pixel dwell time, and $\hat{I}_{STED}^{max} = 4.7$ GW/cm^2. Whereas the confocal recording (Fig. 2 *a* and *e*) yielded undefined blobs, the STED images (Fig. 2 *b* and *f*) discerned most, if not all, of the 24-nm-diameter beads.

Fig. 2 *g* and *h* depict line profiles through beads located 39 and 42 nm apart, respectively; both are clearly separated. The line profile in Fig. 2*d* also exhibits a small background. Careful dichroic filtering excludes the presence of scattered laser light in the image. Most likely, a fraction of the fluorophore molecules leaked into the mounting medium (Mowiol; Merck, Darmstadt, Germany), a phenomenon commonly observed with larger
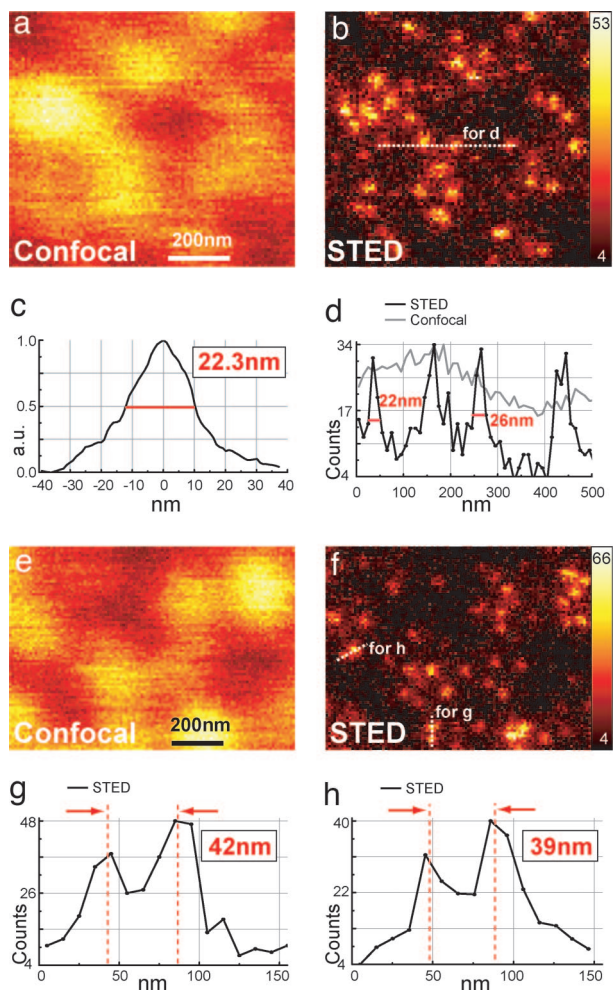
Fig. 2. Resolution ≤20 nm in the focal plane of a STED microscope demonstrated with fluorescent nanobeads. Whereas the confocal imaging mode (*a* and *e*) fails to resolve the bead agglomeration, the corresponding STED recording (*b* and *f*) discerns every 24-nm bead. (*c*) Averaged profile of bead images. The 22.3-nm FWHM indicates a lateral resolution of ≈16 nm in the focal plane (after extraction of the bead size). (*d*) Data as indicated by the dashed line in *b* both for the confocal and the STED recording. Note the sharp peaks resulting from STED superresolution. (*g* and *h*) Intensity profiles through the data in *f* proving the separation capability of the STED microscope.

(>200 nm) fluorescent beads as well. The structure of the fluorophore and its molecular bleaching kinetics remained unknown to us, but, at 80 MHz, resolving beads of this size was virtually precluded by photobleaching. We also determined the function describing the bead image by averaging over 75 beads that were comparatively isolated and of lesser brightness. The result is displayed in Figs. 1*a Right* and 2*c*, exhibiting a FWHM of 22.3 ± 2 nm. Note the striking reduction in size as compared with the diffraction-limited blue excitation spot in Fig. 1*a*.

As it is given by the convolution of the bead object function with the point-spread function (PSF) of the microscope, the bead image function in Fig. 2*c* is just an upper bound for the actual PSF. Therefore, the actual resolution of the STED microscope is <20 nm. If the PSF and the bead function are coarsely approximated by Gaussians, we can assess the actual focal plane resolution as $22.3/\sqrt{2} = 15.8 \pm 4$ nm. Comparison of this value with the resolution limit given by Abbe's criterion in an epifluorescence microscope, $\lambda_{Fl}/2n \sin \alpha = 190$ nm, demonstrates a ≈12-fold gain in resolution in any direction within the focal plane.

Next, we exemplified the resolution of T-Rex STED microscopy with biological immunofluorescence imaging (20). To this end, we labeled secondary antibodies with Atto532, which were then coupled, via primary antibodies, to the proteins of interest. Fig. 3 compares recordings of synaptotagmin I, a transmembrane synaptic vesicle protein, on purified endosomes of the pheochromocytoma-derived PC12 cell line (21). Whereas the confocal image (Fig. 3*a*) displays diffraction-limited blobs of 192 nm FWHM (Fig. 3*c*), the corresponding STED image ($I^{max}_{STED} = 1.6$ GW/cm^2) identifies protein patches in the range of 25–40 nm. The endosomes themselves may be much larger, but what is imaged here are their labeled synaptotagmin molecules. Fig. 3*d* shows an intensity profile through such an endosomal protein cluster featuring a FWHM of 27 nm. As with the bead images, the actual resolving power in this image should be better, because the extent of the labeled protein cluster is nonnegligible. We can assess that the molecular distribution of synaptotagmin I on the endosome plus the attached antibodies is at least 15 nm. Therefore, we can conclude that the actual lateral resolution of the system is at least 20 nm.

Containing a variety of synaptic proteins, the endosomes of PC 12 cells have been used extensively in *in vitro* assays for studying neuroendocrine activity; in particular, they have been found to generate synaptic vesicles (21). To this end, the endosomes supposedly form protein subdomains containing just synaptic vesicle proteins, such as synaptophysin. These subdomains subsequently break off. So far, this hypothesis was difficult to put to the test because endosomes are too small to disclose any substructure using fluorescence microscopy. Conversely, the substructures cannot be easily recognized by electron microscopy because of the low efficiency of immunolabeling with metal particles. Fig. 4 shows that STED microscopy displays synaptophysin patterns on endosomes, such as nanosized C-shapes and rings, thus opening up an avenue for the study of vesicle formation.

Next, we directed the superresolving capabilities of STED microscopy to the highly compartmentalized structure of mammalian interphase nuclei (Fig. 5). We were particularly interested in the nuclear "speckles" enriched in premessenger RNA
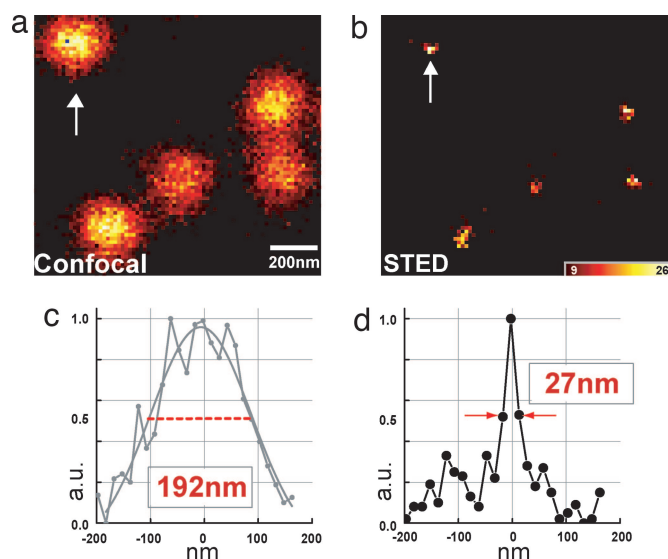

Fig. 3. Synaptotagmin I molecules form distinct spots on endosomes. (*a* and *b*) Whereas confocal microscopy exhibits a 190- to 200-nm diffraction-limited spot per endosome (*a*), STED microscopy recognizes sharp dots of 25–40 nm (*b*), both indicating its resolution as well as the punctated spatial arrangement of synaptotagmin I on the endosome. (*c* and *d*) Corresponding intensity profiles.
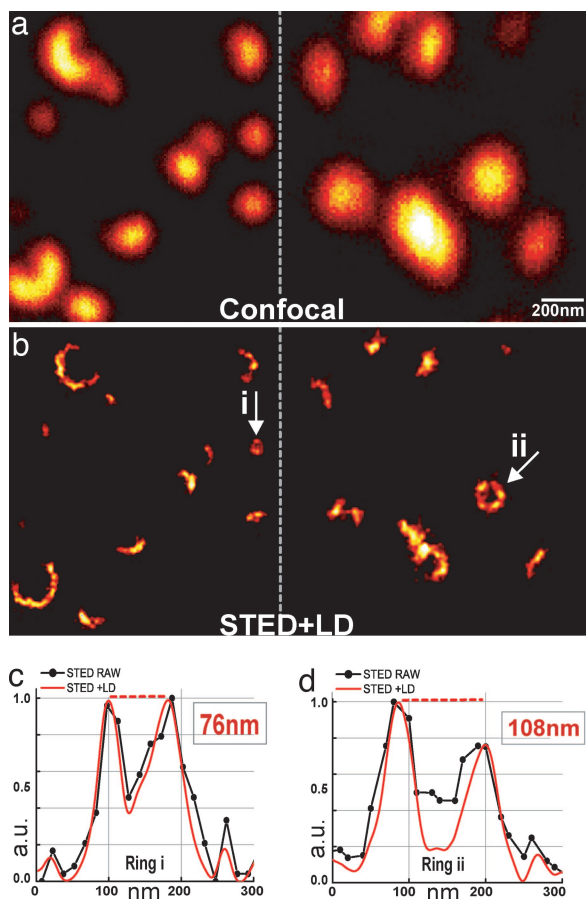
Fig. 4. Synaptophysin forms elaborate nanopatterns on endosomes. (*a*) Confocal reference. (*b*) STED microscopy plus a LD (see *Material and Methods*) revealing ring-like and C-shaped nanoarrangements. (*c* and *d*) Line profiles through rings, both of the LD (red line) and of the raw STED data (black, with pixels).

The intensity profiles in Figs. 3–6 featuring a FWHM of 22–30 nm demonstrate the fundamental progress in resolution brought about by T-Rex STED microscopy. Representing the convolution of the microscope's PSF with the spatial extent of the labeling, the FWHM of the profiles are just an upper limit for the actual imaging resolution. In fact, with a complex size of 6–8 nm, the secondary antibodies form an estimated 12- 16-nm diameter volume around the similarly sized primary antibody (28). Thus, the resolution has attained values that are close to the limits set by the labeling itself.

The used doughnut in Fig. 1*a* improves the resolution in the focal plane only. However, a similar resolution should be attainable in the axial direction (*z*) as well. A powerful option to achieve this goal is the synergistic combination of STED with 4Pi microscopy (29, 30). Initial reports of this combination have resulted in a *z*-resolution of ≈30–60 nm. We also note that a further concept based on saturating the fluorescence signal (31, 32) and another one on protein photoswitching (12, 33) have recently been vindicated, sharing with STED the use of a reversible saturable transition. The ability of T-Rex STED microscopy to attain a spatial resolution of 15–20 nm indicates that a similar resolving power may also be attainable with these approaches if the pertinent photobleaching issues are dealt with. Additionally, all these approaches can be combined with photon statistical localization methods (34, 35) to improve the microscopy resolution.

Although we reduced the repetition rate by 320, the extension in recording time was only 5- to 10-fold compared with the 80-MHz case. Because of the stronger signal, the typical dwell time in our images was 3–8 ms per pixel. More importantly, T-Rex does not depend on the use of low-repetition-rate lasers, because this concept can also be realized by fast scanning. If the scan speed is so high that a fluorescent molecule does not encounter successive pulses within the dark-state relaxation
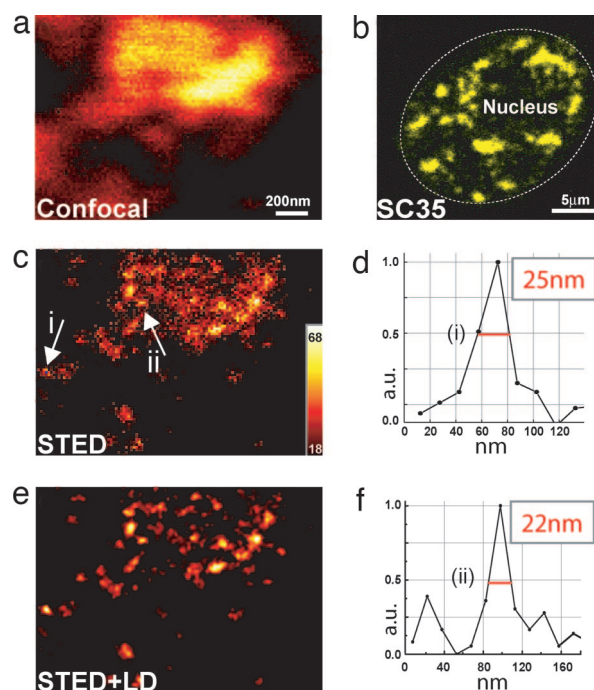
splicing factors and polyadenylated RNA (22–24). We imaged the distribution of a speckle marker protein, SC35, with both confocal and STED microscopy (Fig. 5 *a* and *c*). In contrast to the confocal imaging (24), the resolving power of the STED microscopy allowed us to separate the speckles into distinct particles that have so far been accessible by electron microscopy only (25). In Fig. 5*e*, the speckle nanostructures are further highlighted by applying a one-step linear deconvolution (LD) (see *Material and Methods*). Fig. 5 *d* and *f* shows a raw data profile of two of the substructures. Featuring a FWHM values of 25 and 22 nm, respectively, the profiles prove that the ≈20-nm resolution also is obtained in the nucleus of a fixed but otherwise intact mammalian cell. T-Rex STED microscopy thus appears to be suitable to bring further critical insight into how the nuclear organization ensures regulated gene expression.

Fig. 6 displays the protein-heavy subunit of neurofilaments in the human neuroblastoma cell line SH-SY5Y (retinoic acid–BDNF-differentiated), which establishes cross-links to organize and stabilize neurofilaments in axons (26). Neurofilaments play an essential role in many neurodegenerative diseases, such as Parkinson's. In contrast to the confocal image (*a*), the STED image (*b*) identifies neurofilamental substructures of 20–30 nm. This is particularly apparent in Fig. 6*d*, which shows a partial area of Fig. 6*b* at a larger magnification and in Fig. 6*e*, where the details are further enhanced by a LD (27). The line plots of raw data in Fig. 6*f* prove that substructures that are only 45 nm apart are separated by a dip of 50%.

Fig. 5. Resolving the nanostructure of speckles of protein SC35 in intact mammalian cell nuclei. (*a*, *c*, and *e*) Confocal image of a speckle domain (*a*) with STED counterpart data, raw (*c*) and after LD (*e*). (*b*) Conventional overview image of speckles in nucleus. (*d* and *f*) Raw data profiles through speckle nanofeatures indicate a STED microscopy lateral resolution of ≈20 nm in the nucleus.
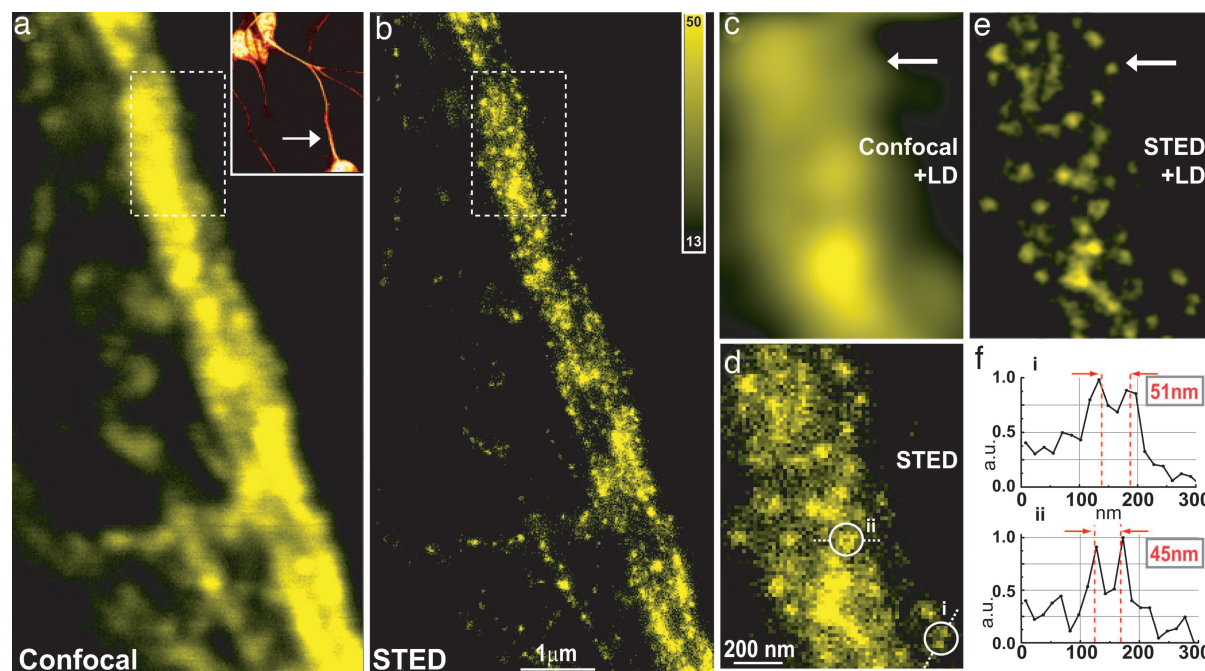
Fig. 6. Imaging neurofilaments in human neuroblastoma. (*a Inset*) Low-magnification confocal image indicates the site of recording. (*a–d*) Contrary to the confocal recording (*a*), the STED recording (*b*) displays details <30 nm, as also highlighted by the comparison of image subregions shown in *c* and *d* bordered by dashed lines in *a* and *b*, respectively. (*c* and *e*) Subregion after LD. Note that the deconvolved confocal image does not yield a substantial gain in information. (*f*) Profiles of raw data demonstrate the ability of (undeconvolved) STED data to reveal object structures that are far below the wavelength of light.

time, the same protective effect is attained. Therefore, an equivalent T-Rex approach is the speed of the scanning spot across the specimen exceeding the speed given by the spot size times the pulse repetition rate, e.g., 200 nm × 80 MHz = 16 μm/μs. A compelling advantage of fast scanning is that, unlike with a reduced repetition rate, the idling time of the fluorescent sample is not increased. In fact, by taking advantage of the factor given by the net signal gain, the recording time can be reduced even beyond the typical recording time that is connected with the 80-MHz illumination.

We have briefly screened a number of dyes and have observed the beneficial effects of T-Rex applied to most of the dyes investigated. We also found that this illumination strategy has major implications for other commonly applied pulsed-mode illumination schemes, such as multiphoton excitation and fluorescence lifetime imaging. Furthermore, we note that a significant signal increase also is anticipated if a molecule encounters so few excitation pulses (e.g., 2–10) that a substantial T_1 built-up is effectively precluded. Therefore, the radical reduction of the pulse repetition rate to 0.25 MHz chosen in this study is not strictly required. In other words, a repetition rate of a few MHz should also lead to a substantial signal increase. Reduction of the repetition rate and fast scanning can also be combined to great effect. Hence, our results not only signify a fundamental increase in signal and resolution but should open the door to far-field optical recording of live cellular organelles at the nanoscale. Besides, it should also be possible to extend STED microscopy to two-color labeling, thus greatly facilitating studies of protein colocalization at the nanoscale.

Finally, we note that the attained far-field optical resolution is similar to that of current high-end x-ray microscopy (36). In contrast to the latter, STED has the potential to provide 3D images without tomography and, what is perhaps more important, can harness fluorescence labeling. Moreover, our results show that lens-based fluorescence microscopy has reached macromolecular-scale resolution. We expect this arguably unex-

pected power of light microscopy to unravel many fundamental problems in the life sciences in the near future.

Materials and Methods

Imaging and Deconvolution. Imaging and deconvolution were performed by scanning the focal spot through the specimen using a piezo stage (Melles Griot, Cambridge, U.K.) with pixel sizes of 10 nm (in Fig. 2) and 15 nm (Figs. 3–6). A single-step LD, i.e., Wiener filter, was carried out where indicated with a theoretical PSF assuming a FWHM of 20 nm. Noise-induced negative values <10% of the image maximum were clipped.

Endosome Preparation from PC12 Cells (Figs. 3 and 4). Cells (clone 251) were grown to ≈70% confluence in DMEM supplemented with 5% FCS, 10% horse serum, 4 mM glutamine, and 100 units/ml penicillin/streptomycin. Early endosomes were purified from postnuclear supernatant by discontinuous sucrose gradient centrifugation (we collected the endosome band at the 35–25% sucrose interface) and centrifuged onto BSA-coated coverslips (40 min at 5,900 × *g* in a Multifuge4 centrifuge; Heraeus, Hanau, Germany). The endosomes were then fixed with 4% paraformaldehyde for 20 min. Primary antibodies (anti-synaptophysin, Cl 7.2, and anti-synaptotagmin1, Cl 41.1; Synaptic Systems, Göttingen, Germany) were then applied at a dilution of 1:100, for 1 h in PBS containing 1.5% BSA. Coverslips were washed three times with PBS, incubated with sheep anti-mouse Atto 532-labeled secondary antibodies for 90 min, washed with PBS containing 500 mM NaCl, embedded in Mowiol, and imaged.

Labeling of SC35 Protein in Nucleus (Fig. 5). HeLa SS6 cells were grown on glass coverslips (FisherScientific, Schwerte, Germany) in DMEM (GibcoBRL, Gaithersburg, MD) supplemented with 10% FCS (GibcoBRL) and 100 units·ml^{-1} penicillin/streptomycin (Biochrom, Berlin, Germany) at 37°C in 5% CO_2. The cells were then washed with PBS, fixed for 20 min with PBS,

pH 7.4/4% (wt/vol) paraformaldehyde, rinsed with PBS (pH 7.4), and permeabilized in PBS, pH 7.4/0.2% Triton X-100 (Sigma, Munich, Germany) for 20 min. The cells were then rinsed with PBS, blocked in PBS, pH 7.4/10% FCS for 30 min, and incubated for 60 min with the mouse anti-SC35 antibody (catalog no. 556363; BD Pharmingen, San Diego, CA) diluted 1:500 in PBS pH 7.4/10% FCS. Subsequently, cells were washed and incubated overnight with the secondary Atto532-labeled antibody at 4°C. The coverslips were again washed and mounted in Mowiol.

Neurofilaments (Fig. 6). The SH-SY5Y neuroblastoma cell line was grown as previously described (26). Cells were seeded on standard glass coverslips to a confluency of ≈80%. *All-trans*-retinoic acid (RA) at 10 μM (EMD Biosciences, San Diego, CA) was added the day after plating. After 5 days in the presence of *all-trans*-retinoic acid, cells were washed three times and incubated with 50 ng/ml human BDNF (Alomone Laboratories, Jerusalem, Israel) in serum-free medium. Immunostaining of neurofilaments as a neuronal marker protein was performed with anti-200kD neurofilament-heavy subunit rabbit IgG (Abcam, Cambridge, U.K.) as the primary antibody and with anti-rabbit-conjugated Atto 532 IgG as the secondary antibody. The cells were mounted in Mowiol.

1. Abbe, E. (1873) *Arch. Mikrosk. Anat. Entwicklungsmech.* **9,** 413–420.
2. Hell, S. W. (1994) *Opt. Commun.* **106,** 19–22.
3. Hell, S. W. & Wichmann, J. (1994) *Opt. Lett.* **19,** 780–782.
4. Klar, T. A. & Hell, S. W. (1999) *Opt. Lett.* **24,** 954–956.
5. Klar, T. A., Jakobs, S., Dyba, M., Egner, A. & Hell, S. W. (2000) *Proc. Natl. Acad. Sci. USA* **97,** 8206–8210.
6. Sieber, J. J., Willig, K. I., Heintzmann, R., Hell, S. W. & Lang, T. (2006) *Biophys. J.* **90,** 2843–2851.
7. Willig, K. I., Rizzoli, S. O., Westphal, V., Jahn, R. & Hell, S. W. (2006) *Nature* **440,** 935–939.
8. Kittel, R. J., Wichmann, C., Rasse, T. M., Fouquet, W., Schmidt, M., Schmid, A., Wagh, D. A., Pawlu, C., Kellner, R., Willig, K. I., *et al.* (2006) *Science* **312,** 1051–1054.
9. Einstein, A. (1917) *Physik. Zeitschr.* **18,** 121–128.
10. Schäfer, F. P. (1973) *Dye Lasers* (Springer, Berlin).
11. Denk, W., Strickler, J. H. & Webb, W. W. (1990) *Science* **248,** 73–76.
12. Hell, S. W. (2003) *Nat. Biotechnol.* **21,** 1347–1355.
13. Westphal, V. & Hell, S. W. (2005) *Phys. Rev. Lett.* **94,** 143903.
14. Eggeling, C., Widengren, J., Rigler, R. & Seidel, C. A. M. (1998) *Anal. Chem.* **70,** 2651–2659.
15. Hopt, A. & Neher, E. (2001) *Biophys. J.* **80,** 2029–2036.
16. Dyba, M. & Hell, S. W. (2003) *Appl. Optics* **42,** 5123–5129.
17. Eggeling, C., Volkmer, A. & Seidel, C. A. M. (2005) *ChemPhysChem* **6,** 791–804.
18. Kasha, M. (1960) *Rad. Res.*, Suppl. 2, 243–275.
19. Torok, P. & Munro, P. R. T. (2004) *Opt. Expr.* **12,** 3605–3617.
20. Weber, K., Rathke, P. C. & Osborn, M. (1978) *Proc. Natl. Acad. Sci. USA* **75,** 1820–1824.
21. Lichtenstein, Y., Desnos, C., Faundez, V., Kelly, R. B. & Clift-O'Grady, L. (1998) *Proc. Natl. Acad. Sci. USA* **95,** 11223–11228.
22. Spector, D. L. (1993) *Annu. Rev. Cell Biol.* **9,** 265–315.
23. Misteli, T. & Spector, D. L. (1998) *Curr. Opin. Cell Biol.* **10,** 323–331.
24. Mintz, P. J. & Spector, D. L. (2000) *J. Struct. Biol.* **129,** 241–251.
25. Monneron, A. & Bernhard, W. (1969) *J. Ultrastruct. Res.* **27,** 266–288.
26. Yuan, A., Nixon, R. A. & Rao, M. V. (2006) *Neurosci. Lett.* **393,** 264–268.
27. Tikhonov, A. N. & Arsenin, V. Y. (1977) *Solutions of Ill-Posed Problems* (Wiley, New York).
28. Osborne, M. (1998) in *Cell Biology: A Laboratory Handbook*, ed. Celis, J. E. (Academic, San Diego), Vol. 2, pp. 462–468.
29. Dyba, M. & Hell, S. W. (2002) *Phys. Rev. Lett.* **88,** 163901.
30. Dyba, M., Jakobs, S. & Hell, S. W. (2003) *Nat. Biotechnol.* **21,** 1303–1304.
31. Gustafsson, M. G. L. (2005) *Proc. Natl. Acad. Sci. USA* **102,** 13081–13086.
32. Heintzmann, R., Jovin, T. M. & Cremer, C. (2002) *J. Opt. Soc. Am. A* **19,** 1599–1609.
33. Hofmann, M., Eggeling, C., Jakobs, S. & Hell, S. W. (2005) *Proc. Natl. Acad. Sci. USA* **102,** 17565–17569.
34. Michalet, X. & Weiss, S. (2006) *Proc. Natl. Acad. Sci. USA* **103,** 4797–4798.
35. Ram, S., Ward, E. S. & Ober, R. J. (2006) *Proc. Natl. Acad. Sci. USA* **103,** 4457–4462.
36. Chao, W. L., Harteneck, B. D., Liddle, J. A., Anderson, E. H. & Attwood, D. T. (2005) *Nature* **435,** 1210–1213.

APPLIED PHYSICAL SCIENCES

BIOPHYSICS